



# Simulation of CO<sub>2</sub> Storage Using a Parameterization Method for Essential Trapping Physics: FluidFlower Benchmark Study

Yuhang Wang<sup>1,2,3</sup> · Ziliang Zhang<sup>2,3</sup> · Cornelis Vuik<sup>2</sup> · Hadi Hajibeygi<sup>3</sup>

Received: 30 November 2022 / Accepted: 24 June 2023  
© The Author(s) 2023

## Abstract

An efficient compositional framework is developed for simulation of CO<sub>2</sub> storage in saline aquifers during a full-cycle injection, migration and post-migration processes. Essential trapping mechanisms, including structural, dissolution, and residual trapping, which operate at different time scales, are accurately captured in the presented unified framework. In particular, a parameterization method is proposed to efficiently describe the relevant physical processes. The proposed framework is validated by comparing the dynamics of gravity-induced convective transport with that reported in the literature. Results show good agreement for both the characteristics of descending fingers and the associated dissolution rate. The developed simulator is then applied to study the FluidFlower benchmark model. An experimental setup with heterogeneous geological layers is discretized into a two-dimensional computational domain where numerical simulation is performed. Impacts of hysteresis and the diffusion of CO<sub>2</sub> in liquid phase on the migration and trapping of CO<sub>2</sub> plume are investigated. Inclusion of the hysteresis effect does not affect plume migration in this benchmark model, whereas diffusion plays an important role in promoting convective mixing. This work casts a promising approach to predict the migration of the CO<sub>2</sub> plume, and to assess the amount of trapping from different mechanisms for long-term CO<sub>2</sub> storage.

**Keywords** Geological CO<sub>2</sub> storage · Porous media · Compositional simulation · Convective mixing · Hysteresis

---

✉ Yuhang Wang  
wangyuhang17@cug.edu.cn

✉ Ziliang Zhang  
z.zhang-15@tudelft.nl

✉ Cornelis Vuik  
c.vuik@tudelft.nl

✉ Hadi Hajibeygi  
h.hajibeygi@tudelft.nl

<sup>1</sup> School of Environmental Studies, China University of Geosciences, Wuhan 430078, China

<sup>2</sup> Faculty of Electrical Engineering, Mathematics and Computer Science, Department of Applied Mathematics, Delft University of Technology, Delft 2628XE, The Netherlands

<sup>3</sup> Faculty of Civil Engineering and Geosciences, Department of Geoscience and Engineering, Delft University of Technology, Delft 2628CV, The Netherlands

## 1 Introduction

Carbon dioxide capture and storage (CCS) is one of the promising measures to reduce greenhouse gas emission, and mitigate the climate change (Krevor et al. 2023). This technique usually consists of subsequent processes, including collection of CO<sub>2</sub> emission from large point source like power plants, transportation of the collected gas emission, and storing it in geological formations (Metz et al. 2005). Of potential geological targets, deep saline aquifers are of great importance because they are prevalent in sedimentary basins and have promising storage capacity. However, the spatial heterogeneity in geological formations, as well as high contrast between fluids when storing CO<sub>2</sub> in saline aquifers, pose challenges in understanding and simulating such unstable processes (Wang et al. 2019; Ershadnia et al. 2020; Jackson and Krevor 2020; Yang et al. 2020; Zheng et al. 2021; Boon et al. 2022; Kou et al. 2022; Shao et al. 2022).

The well-classified trapping mechanisms, by which injected CO<sub>2</sub> can be sequestered in pore spaces, include structural and stratigraphic trapping (Szulczewski et al. 2013; Emami-Meybodi et al. 2015), residual trapping (Hunt et al. 1988; Juanes et al. 2006; Herring et al. 2013), dissolution trapping (Duan and Sun 2003; Spycher et al. 2003; Spycher and Pruess 2005), and mineral trapping (Dai et al. 2020; Snæbjörnsdóttir et al. 2020). Structural and stratigraphic trapping is the part of CO<sub>2</sub> trapped by an overlying impermeable (or low-permeability) seal as CO<sub>2</sub> migrates in the reservoir. Specifically, structural trap is formed by tectonic processes after the deposition of the reservoir bed, whereas the stratigraphic trap is created during the deposition period. Residual trapping, also known as capillarity trapping, applies to the CO<sub>2</sub> that is left behind and loses its spatial continuity when water reinvades into pore space occupied by CO<sub>2</sub>. Such trapping occurs mostly in areas near wellbore and plumes spreading under caprock after injection stops. Dissolution trapping occurs when CO<sub>2</sub> and brine are in contact with each other during injection and migration. The amount of CO<sub>2</sub> which can be dissolved into brine relies on pressure, temperature, and salinity of brine; their effects on CO<sub>2</sub> dissolubility have been extensively studied in the literature. Mineral trapping refers to the process during which CO<sub>2</sub> is precipitated as carbonate minerals and trapped in a more permanent form. The rate of geochemical reaction depends on the host rock. For instance, mineralization happens rapidly in basalt due to its high concentration of divalent cations. However, it can take thousands of years for all injected CO<sub>2</sub> to be mineralized in sandstone. In this case, mineral trapping may not act effectively in the short term.

The relative importance of different trapping mechanisms varies temporally (Ide et al. 2007). Consider the full-cycle CO<sub>2</sub> storage in a sandstone aquifer with a relatively gentle inclination. As governed by advective transport during injection period, structural trapping dominates the contribution to stored CO<sub>2</sub> at early stage. Residual trapping comes into effect when injection stops, since most transitions of the displacement process, i.e., from drainage to imbibition, take place at this point in time. The above two trapping mechanisms operate at a time scale close to injection period, while the dissolution trapping lasts longer (Wang et al. 2022). Dissolution occurs in regions swept by CO<sub>2</sub> during injection and continues to play a crucial role due to the gravity-induced convective transport in post-injection period (Ranganathan et al. 2012; Emami-Meybodi and Hassanzadeh 2015; De Paoli et al. 2017; Wen et al. 2021). Obviously, mineral trapping operates at a even larger time scale than dissolution because of the slow reaction kinetics (Gunter et al. 2000). In order to evaluate the interplay of those trapping mechanisms, it is of necessity to develop an efficient and robust numerical framework. One of the challenging tasks is to capture the hysteresis

effect. Especially in the CO<sub>2</sub>-brine system, the hysteretic behavior of relative permeability and capillary pressure has already been revealed by experimental studies (Oak et al. 1990; Akbarabadi and Piri 2013; Ruprecht et al. 2014; Pini and Benson 2017), and mathematical models were proposed to determine residual gas saturation based on the history of saturation (Land 1968; Steffy et al. 1997).

Efforts have been made to investigate CO<sub>2</sub> storage using numerical models. In most case, simulations are conducted at field-scale and coarse grids are often employed (Class et al. 2009; Nordbotten et al. 2012). In consequence, the numerical error, as well as the spatial heterogeneity may overwhelm the relevant physical processes, and it is impractical to compare the simulation results with any physical observations. The FluidFlower benchmark study provides an excellent opportunity to examine the predictive capability of the Darcy-scale model, and to study the interactions of underlying physics, some of which may be neglected at field-scale (e.g., CO<sub>2</sub> diffusion in liquid phase), in a comprehensive manner. The experiment is designed to mimic CO<sub>2</sub> storage in a layered system using a meter-scale rig. Physical parameters of different sand types are measured which will be used in the simulation. The uncertainty arising from either spatial heterogeneity or physical properties are well-regulated, allowing for a direct comparison between numerical predictions and experimental observations.

This work is structured as follows. we first present the governing equations describing the CO<sub>2</sub>-brine system, thermodynamic equilibrium calculation, and the solution strategy. Following that we show how physical models are parameterized to improve the computational efficiency. The proposed compositional framework is validated by investigating the gravity-induced convective transport. Next, we present simulation results of FluidFlower benchmark model and discuss the impacts of key physical processes on plume migration and trapping of CO<sub>2</sub>. Key findings are summarized at the end.

## 2 Methodology

### 2.1 Compositional Formulation

The governing equation describing a multi-component, multi-phase flow system is given by:

$$\frac{\partial}{\partial t} \left( \phi \sum_{\alpha=1}^{n_{\text{ph}}} x_{c,\alpha} \rho_{\alpha} S_{\alpha} \right) + \nabla \cdot \sum_{\alpha=1}^{n_{\text{ph}}} (x_{c,\alpha} \rho_{\alpha} u_{\alpha} + S_{\alpha} \rho_{\alpha} J_{c,\alpha}) = \sum_{\alpha=1}^{n_{\text{ph}}} x_{c,\alpha} \rho_{\alpha} q_{\alpha}, \quad (1)$$

where subscript  $\alpha$  represents liquid (brine) or gas (supercritical CO<sub>2</sub>) phase, and  $c$  denotes the component, i.e., brine or CO<sub>2</sub> in this case.  $\phi$  is rock porosity;  $\rho_{\alpha}$ ,  $S_{\alpha}$ , and  $q_{\alpha}$  are the molar (mass) density, saturation, and flow rate of phase  $\alpha$ , respectively. Note that  $x_{c,\alpha}$  is the molar (mass) fraction of component  $c$  in phase  $\alpha$ .  $u_{\alpha}$  is the phase velocity and described by the classic extension of Darcy's law:

$$u_{\alpha} = \frac{kk_{r,\alpha}}{\mu_{\alpha}} \nabla (p_{\alpha} - \rho_{\alpha} gh), \quad (2)$$

where  $k$  is the rock permeability;  $k_{r,\alpha}$  and  $\mu_{\alpha}$  are phase relative permeability and viscosity, respectively.  $J_{c,\alpha}$  is the diffusive flux in phase  $\alpha$ . According to Fick's law,  $J_{c,\alpha}$  is proportional to the gradient of molar (mass) fraction given by

$$J_{c,\alpha} = -\phi D_{c,\alpha} \nabla x_{c,\alpha}, \tag{3}$$

where  $D_{c,\alpha}$  is the diffusion coefficient of component  $c$  in phase  $\alpha$ .

### 2.2 Overall-Compositional Formulation

In our two-component two-phase system, the overall composition variable set is chosen to solve the system of nonlinear equations, using phase pressure and overall molar fraction as primary variables (Voskov and Tchelepı 2012). The overall mole fraction of component  $c$ ,  $z_c$ , is defined as:

$$z_c = \sum_{\alpha=1}^{n_{ph}} v_{\alpha} x_{c,\alpha}, \quad \forall c \in 1, \dots, n_c \tag{4}$$

where  $v_{\alpha} = S_{\alpha} \rho_{\alpha} / (\sum_{\alpha=1}^{n_{ph}} S_{\alpha} \rho_{\alpha})$  represents the molar (mass) fraction of phase  $\alpha$ . With the defined overall molar fraction term, the mass conservation equation for each component can be rewritten as:

$$\frac{\partial}{\partial t} (\phi \rho_T z_c) + \nabla \cdot \sum_{\alpha=1}^{n_{ph}} (x_{c,\alpha} \rho_{\alpha} u_{\alpha} + S_{\alpha} \rho_{\alpha} J_{c,\alpha}) = \sum_{\alpha=1}^{n_{ph}} x_{c,\alpha} \rho_{\alpha} q_{\alpha}, \tag{5}$$

here  $\rho_T$  denotes the total density, and it is a function of phase density and saturation.

### 2.3 Analytical Flash Calculation

When multiple phases are present, it is usually assumed that all phases reach thermodynamic equilibrium instantaneously to decouple phase behavior calculation from flow (Cusini et al. 2018). In this work, we consider a black-oil type fluid model which allows the lighter component to exist in both phases. This model is suitable for an isothermal system without significant change in thermodynamic conditions (Hassanzadeh et al. 2008). The equilibrium ratio, also known as the  $k$ -value, determines how one component is split into different phases:

$$k_c = \frac{x_{c,g}}{x_{c,l}}. \tag{6}$$

The phase constraints based on molar fraction terms read:

$$\sum_{c=1}^{n_c} x_{c,\alpha} = 1, \quad \sum_{c=1}^{n_{ph}} v_{\alpha} = 1. \tag{7}$$

Based on the definition of the overall molar fraction term, phase distribution parameters can be derived analytically as:

$$\begin{bmatrix} x_{CO_2,g} & x_{b,g} & V \\ x_{CO_2,l} & x_{b,l} & L \end{bmatrix} = \begin{bmatrix} 1 & 0 & \frac{z_{CO_2} - \frac{1}{k_{CO_2}}}{1 - \frac{1}{k_{CO_2}}} \\ \frac{1}{k_{CO_2}} & 1 - \frac{1}{k_{CO_2}} & \frac{1 - z_{CO_2}}{1 - \frac{1}{k_{CO_2}}} \end{bmatrix}. \tag{8}$$

## 2.4 Solution Strategy

The nonlinear system of equations is solved using finite volume discretization in space and implicit discretization in time. The nonlinear equation for component  $c$  in cell  $i$  in residual form can be linearized with the Newton–Raphson method as:

$$r_{c,i}^{v+1} \approx r_{c,i}^v + \left( \frac{\partial r_{c,i}}{\partial p_l} \right)^v \delta p_l^{v+1} + \left( \frac{\partial r_{c,i}}{\partial z_{\text{CO}_2}} \right)^v \delta z_{\text{CO}_2}^{v+1} = 0, \quad (9)$$

here  $v$  and  $v + 1$  are the current and next iteration step, respectively. Then the linearized equations are solved in an iterative manner:

$$J^v \delta x^{v+1} = -r^v, \quad (10)$$

where  $J^v$  and  $r^v$  are Jacobian and Residual matrix, and  $\delta x^{v+1}$  is the primary variable update. The same function in matrix multiplication form is given below:

$$\begin{pmatrix} \frac{\partial r_{\text{CO}_2}}{\partial p_l} & \frac{\partial r_{\text{CO}_2}}{\partial z_{\text{CO}_2}} \\ \frac{\partial r_b}{\partial p_l} & \frac{\partial r_b}{\partial z_{\text{CO}_2}} \end{pmatrix} \begin{pmatrix} \delta p_l \\ \delta z_{\text{CO}_2} \end{pmatrix} = - \begin{pmatrix} r_{\text{CO}_2} \\ r_b \end{pmatrix}. \quad (11)$$

The process is repeated until it reaches nonlinear convergence, i.e., the infinite norm of the residual and variable update are less than a certain tolerance. In addition, an adaptive time stepping strategy is employed to reduce the number of iterations needed to reach convergence. In the implementation, the time step size is dynamically changed between user defined maximum and minimum time step size, based on the number of iterations needed to converge.

## 3 Parameterized Physical Models

### 3.1 Dissolution

The solubility of CO<sub>2</sub> in brine varies with pressure, temperature and water salinity (Spycher et al. 2003). In this work, the volume of CO<sub>2</sub> that can be dissolved into a unit volume of brine is quantified by the solution CO<sub>2</sub>-brine ratio, or  $R_s$ , at given temperature and salinity. As a result,  $R_s$  depends on pressure only. The corresponding parameterization space can be readily extended across different temperature and salinity settings nevertheless.

We follow a thermodynamic model that equates chemical potential to predict the dissolution of CO<sub>2</sub> (Spycher et al. 2003; Hassanzadeh et al. 2008). The solution CO<sub>2</sub>-brine ratio is calculated using the mole fraction of CO<sub>2</sub> in liquid phase obtained from the CO<sub>2</sub> molality in brine as:

$$R_s = \frac{\rho_b^{\text{STC}} x_{\text{CO}_2,l}}{\rho_{\text{CO}_2}^{\text{STC}} (1 - x_{\text{CO}_2,l})}. \quad (12)$$

Here STC is short for standard condition. The relationship between CO<sub>2</sub> molality and pressure is verified by comparing the calculated data against those obtained using the full solubility model (Duan and Sun 2003). For more details, readers are referred to Wang et al. (2022). CO<sub>2</sub> molality is then converted to the solution ratio, which is stored in a lookup table in the offline stage. The  $R_s$  value can be directly read from the table with known pressure.

It is worth mentioning that the lookup table only applies to cells in two-phase state, i.e., CO<sub>2</sub> exists in both gas and liquid phases. Therefore, a stability test needs to be performed to check the number of phases in each cell after updating the primary variables at each iteration. Assuming brine presents in liquid phase only, the  $k$ -values for CO<sub>2</sub> and brine are given by:

$$k_{\text{CO}_2} = \frac{\rho_{\text{CO}_2}^{\text{STC}} R_s + \rho_b^{\text{STC}}}{\rho_{\text{CO}_2}^{\text{STC}} R_s}, \quad k_b = 0. \quad (13)$$

Here  $k$ -value denotes the mole fraction of a component  $c$  in vapor and liquid phase and will be used to perform stability check. If a cell is in the state of liquid phase solely, the amount of CO<sub>2</sub> dissolved in brine is not enough to reach the dissolution limit (Hajibeygi and Tchelepi 2014). In other words, the solution CO<sub>2</sub>-brine ratio needs to be modified with the overall molar fraction of CO<sub>2</sub> given by:

$$R_s = \frac{\rho_b^{\text{STC}} z_{\text{CO}_2}}{\rho_{\text{CO}_2}^{\text{STC}} (1 - z_{\text{CO}_2})}. \quad (14)$$

Note that if evaporation of liquid phase is considered,  $k_b$  can be nonzero. In that case, a negative flash calculation is usually implemented where  $k$ -values are obtained in a iterative manner (Lyu et al. 2021).

### 3.2 Hysteresis

The hysteresis effect refers to the behavior that different constitutive relations, i.e., relative permeability and capillary pressure curves, are followed depending on the type of on-going process, i.e., drainage or imbibition. When flow transition occurs, a scanning curve will be created at the turning point to ensure the transition is continuous (Kilgough 1976). During the course of a simulation, the scanning curve for each cell is constructed independently, and process of flow is determined by comparing gas saturation from the previous two time steps (Wang et al. 2022),  $n$  and  $(n - 1)$ . For example, if one finds  $S_g^n < S_g^{n-1}$  on primary drainage process, it indicates flow has already been transitioned to imbibition at  $S_g^{n-1}$  (referred to as turning point) shown in Fig. 1a.

As mentioned earlier, the scanning curves were constructed cell by cell in previous work, which may lead to repetitive construction for cells with identical saturation and turning point. To improve the computational efficiency, a parameterized surface is constructed based on the scanning curves created from different turning points—see Fig. 2. Once the primary drainage and imbibition curves (also known as bounding curves) are determined, the surface is established in the offline stage. This is a generic treatment which can be applied to any type of rock under different reservoir conditions.

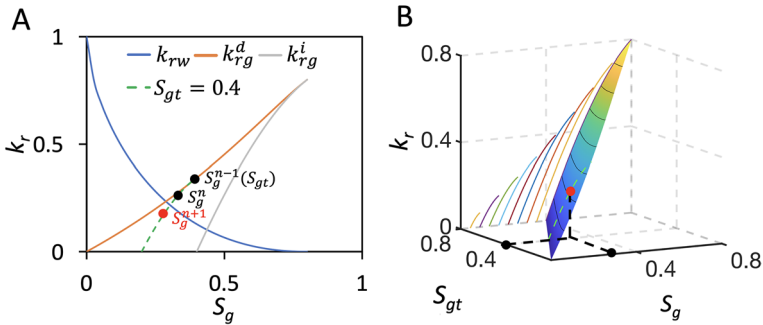


**Fig. 1** Illustration of hysteretic relative permeability models. Evaluation of relative permeability based on **a** a scanning curve, and **b** the scanning curve surface

In the newly proposed workflow, flow process of each cell is determined in a vectorized manner without looping each cell. Relative permeability (or capillary pressure) is obtained directly using multilinear interpolation shown in Fig. 1b.

### 3.3 Capillarity

Capillary pressure function below relates the pressure difference between different phases as:

$$p_\alpha - p_\beta = p_{c\alpha,\beta}, \quad \forall \alpha \neq \beta \in 1, \dots, n_{ph}. \tag{15}$$

Capillary pressure plays an important role in plume migration and CO<sub>2</sub> trapping. CO<sub>2</sub> can be collected under structural and stratigraphic traps when the buoyancy forces cannot overcome the capillary forces in the narrow pore throat of caprock. This ensures CO<sub>2</sub> will not enter the overlying pore space. In addition, a portion of CO<sub>2</sub> is left as discontinuous ganglia and becomes immobilized because of capillary forces. This is referred to as residual trapping, which is affected by pore structure and wettability of the rock. As shown by Fig. 2b, capillary pressure and its hysteresis behavior are also captured by the parameterized space.

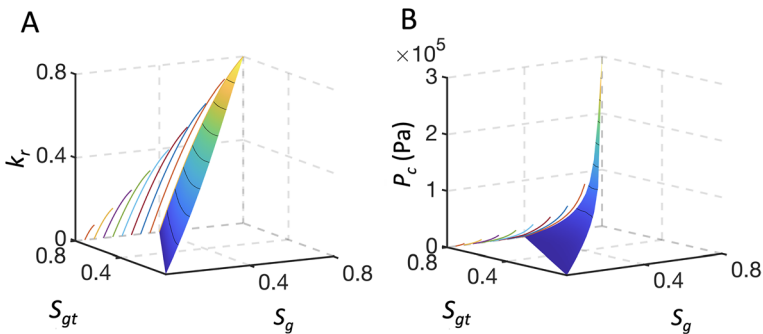


**Fig. 2** Scanning curve surfaces used to model hysteretic constitutive relations. **a** Relative permeability, and **b** capillary pressure

## 4 Validation

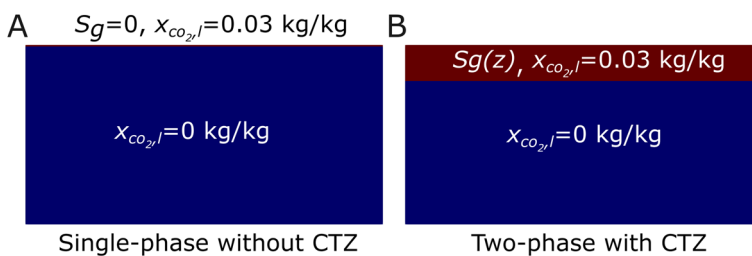
In this section, we validate the proposed compositional framework by investigating a 2D synthetic model. The behavior of gravity-induced convective transport, and the associated dissolution rate in the absence and presence of capillarity transition zone (CTZ) (Elenius et al. 2014, 2015), are studied. Two simulation cases we employ are a) single-phase without CTZ, and b) two-phase with CTZ, which represent negligible and stagnant CTZ scenarios, respectively, (shown in Fig. 3). In the case of single-phase flow (case A), cells of the top boundary have  $\text{CO}_2$  concentration fixed at solubility limit by specifying a large pore volume. On the other hand, cells in the top 10 m of case B are saturated with gaseous  $\text{CO}_2$ . In both cases, no-flow condition is imposed on all boundaries, and the bottom part of domain is fully saturated with single-phase brine at initial stage. The parameters of reservoir and fluid properties are summarized in Elenius et al. (2015).

Figure 4 presents  $\text{CO}_2$  concentration profiles after 200 years in cases A and B. It clearly reveals that CTZ accelerates the propagation of fingers and leads to more pronounced convective transport, as evidenced by further propagation of fingers in case B at 200 years. Moreover, the shape of developed fingers in our results shows good qualitative agreement with those reported in the literature. Specifically, the width of fingers in both cases increases from root to tip with an average value of 5–6 m. Some slightly further development of convective fingers in our simulation results might be attributed to the randomness in perturbation at interfaces (Elenius et al. 2015).

To quantify the interphase mass transfer rate of  $\text{CO}_2$  from gaseous to dissolved phase, a dissolution rate  $F$  is introduced in the literature, which is given by:

$$F = h\phi \frac{\partial \bar{c}}{\partial t}. \quad (16)$$

Here  $h$  and  $\phi$  denote the height and porosity of single-phase brine region, respectively.  $\bar{c}$  is the mean  $\text{CO}_2$  concentration of the same region. Figure 5 indicates that the dissolution rates of both cases follow well with those obtained from the previous study. As shown, the dissolution rate decreases at the early stage because the process is dominated by diffusion. After the so-called onset time,  $F$  starts to increase due to the fact that perturbations grow into descending fingers which enhances the mass flux. The dissolution rate in both cases fluctuates around constant values until fingers reach the bottom of the aquifer. At the end,  $F$  gradually decreases as fingers merge with each other and the driving force for downward transport decreases (Tsinober et al. 2022).



**Fig. 3** Initial fluid distribution of 2D synthetic models used for validation. **a** Single-phase without CTZ, and **b** two-phase with CTZ



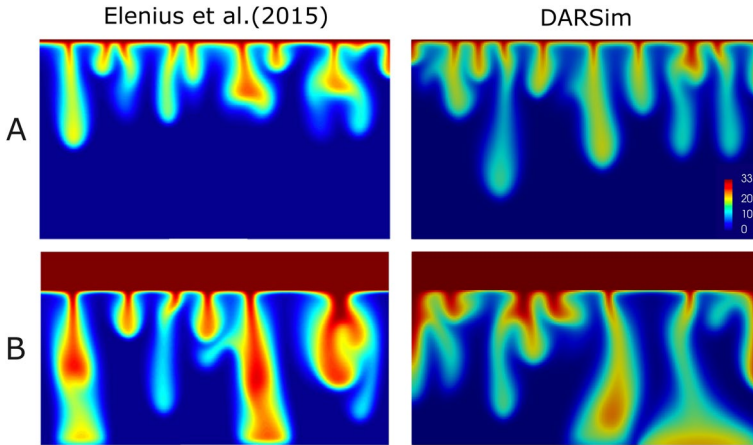


Fig. 4 CO<sub>2</sub> concentration profiles of cases A and B at 200 years

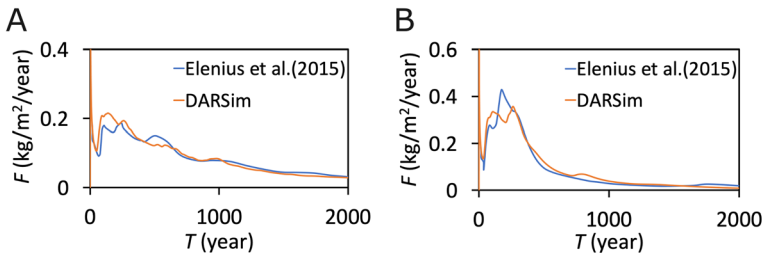


Fig. 5 Dissolution rate of cases A and B over 2000 years

Figure 6 shows the distribution of CO<sub>2</sub> concentration after 250, 350 and 2000 years in the case of two-phase flow, which agree well with the profiles shown in the literature. The associated dissolution rates are also plotted in logarithm scale against the analytical solution. Simulation results fit well with the prediction of analytical solution. Specifically, we found a similar  $t_{\text{peel}}$  of 350 years, before which dissolution rate stabilizes around a constant value. As fingers start propagating along the bottom boundary, dissolution rate decreases and becomes proportional to  $1/t^2$  (Elenius et al. 2015).

## 5 FluidFlower Benchmark Study

The validated compositional framework is applied to study FluidFlower benchmark model. Numerical predictions are compared with experimental observations, and impacts of key physical processes on CO<sub>2</sub> storage are examined.

### 5.1 Model Description

FluidFlower setup is designed to accommodate multiphase flow experiments in 2D and to reproduce key processes happening during CO<sub>2</sub> storage (Flemisch et al. 2023).

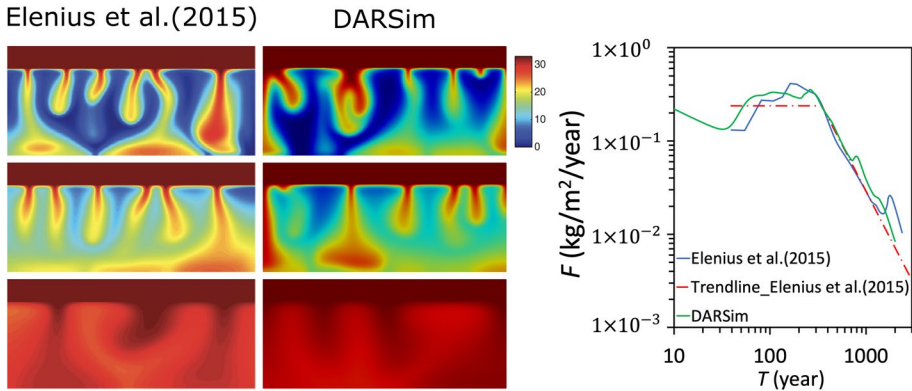


**Fig. 6** CO<sub>2</sub> concentration profiles of case B after 250 (top), 350 (middle), and 2000 (bottom) years, along with the comparison of dissolution rate

A direct visualization of flow dynamics, which is missing from numerical studies, can be delivered. The geometry of geological layers, conceived based on typical North Sea reservoirs, is formed by pouring unconsolidated sand with varying types separately into the water-filled experiment rig. After careful sedimentation operation, the geometry was flushed with different aqueous fluids prior to CO<sub>2</sub> injection. The length and height of the setup are 2.86 m and 1.53 m, respectively, while the width varies between 0.019 and 0.028 m from two sides to the center. Simulations are performed in a 2D domain discretized by  $286 \times 1 \times 153$  cells, assuming the width is fixed at 0.019 m. Figure 7 shows that the geometry used in the experiment is well represented by the discretized model.

Apart from listed petrophysical parameters of different sand types in Table 1, measurements from the tracer test are provided for model calibration (Nordbotten et al. 2022). During the tracer flow, aqueous phases with different colors are injected through two injection ports with a constant volumetric flow rate and square pulses pattern. Permeability values for different sand layers are tuned by a multiplier of 0.5 such that pressure pluses observed at 5 other ports are best represented. Moreover, the best possible match on the horizontal and vertical migration of plume front is found with an anisotropic ratio of 0.9 between horizontal and vertical permeability. Figure 8 shows that the evolution of tracer front agrees well between experimental observations and simulation results with the tuned permeability field.

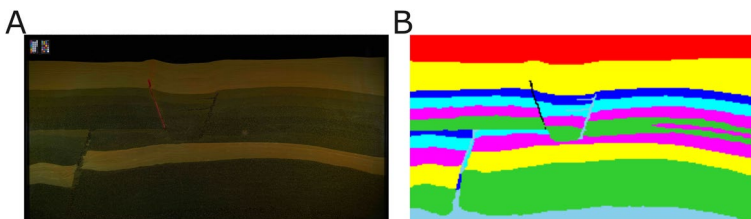


**Fig. 7** Geometry of FluidFlower model. **a** Original geometry, and **b** discretized geometry

**Table 1** Petrophysical parameters of different sand types

id	k[D]	$\phi$	$P_{ce}$	$\lambda$	$k_{rw}^0$	$k_{rg}^0$	$s_{rw}$	$s_{rg}$	Alias
1	1e-6	0.001	0	2	0.71	0.09	0.32	0.14	Barrier
2	9580	0.44	0	2	0.75	0.16	0.10	0.06	G
3	4259	0.45	0	2	0.72	0.11	0.12	0.13	F
4	2005	0.45	0	2	0.93	0.10	0.12	0.06	E
5	1110	0.44	98.1	2	0.95	0.02	0.12	0.08	D
6	473	0.44	294.3	2	0.93	0.05	0.14	0.10	C
7	44	0.43	1471.5	2	0.71	0.09	0.32	0.14	ESF

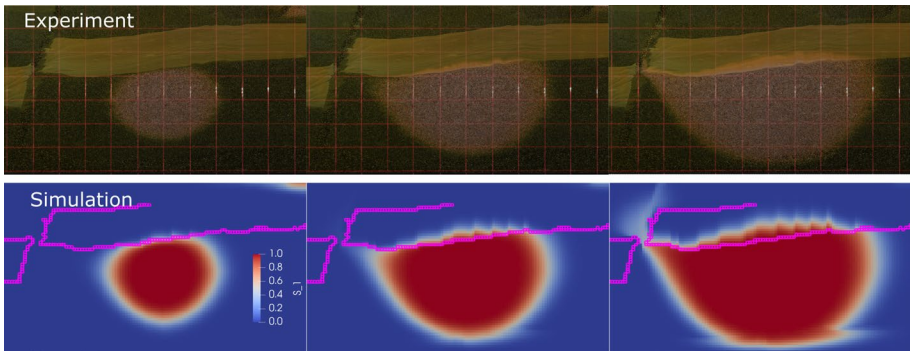


**Fig. 8** Snapshots of tracer test through lower injection port from experiment and simulation (cells representing sealing layer boundaries are highlighted in simulation results)

The relative permeability and capillary pressure curves of different sand types are constructed using the Brooks–Corey model, in which the effective saturation can be computed based on residual saturation values as:

$$S_{ge} = \frac{S_g - S_{gr}}{1 - S_{gr} - S_{wr}} \tag{17}$$

Relative permeability is then calculated by

$$k_{rw} = k_{rw}^0 (1 - S_{ge})^2, \quad k_{rg} = k_{rg}^0 S_{ge}^2 \tag{18}$$

where  $k_{rw}^0$  and  $k_{rg}^0$  are relative permeability end points as listed in Table 1. Similarly, capillary pressure for sand ESF, C and D is given by:

$$P_c = P_{ce} (1 - S_{ge})^{-0.5} \tag{19}$$

Using sand-type ESF as an example, Fig. 9 shows the hysteretic behavior of gas phase while the same curve is used for liquid phase in drainage and imbibition processes. Note that other types of sand are characterized as zero capillarity, which is indicated by the capillary entry pressure shown in Table 1.

Neglecting the thermal effect, the system temperature is assumed to be constant at 20°C. The reservoir is initialized with atmospheric pressure. Particularly, pressure at the top

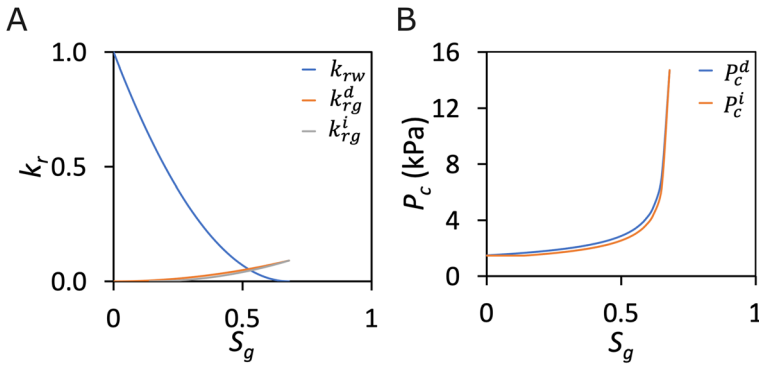


**Fig. 9** Constitutive relation models for sand ESF. **a** Relative permeability, and **b** capillary pressure

boundary is fixed since it is open and is connected to a free water table. No flow occurs across other boundaries. In our study, the injection scheme is implemented following the experimental setting, during which  $\text{CO}_2$  is injected with a constant rate of 10 ml/min through two injection ports for 5 h and 2 h 45 mins, respectively. After injection ceases, simulation continues for 5 days to predict the migration and fate of  $\text{CO}_2$  plume. Fluid properties and some physical parameters used in the simulations are summarized in Table 2.

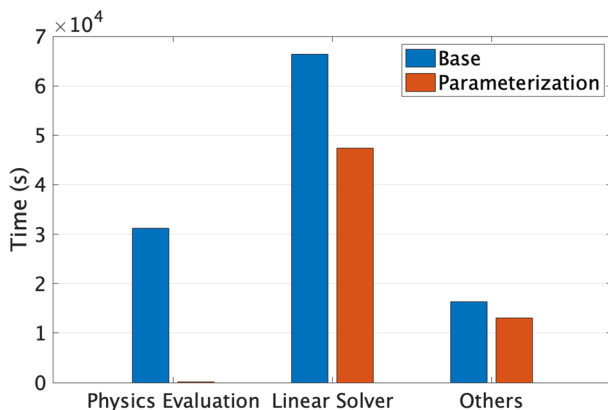
## 5.2 Efficiency Gains

We first present efficiency gains from the proposed parameterization method. As the equilibrium compositional data for  $\text{CO}_2$ -brine system, i.e., solubility of  $\text{CO}_2$  in brine, have been computed and stored before simulation starts, here we focus on the efficiency gains obtained from parameterizing hysteretic constitutive relations. Figure 10 shows the comparison of simulation time spent on physics evaluation, linear solver, and others during the first day from two cases. The (1) Base and (2) Parametrization case refer to simulation runs in which parameterization is unemploye d/implemented, respectively.

It is observed that in the Base case, around 30% of simulation time is spent on evaluating hysteretic constitutive relations, which is saved via the use of parameterized scanning curve surface. Meanwhile, in the case of Parametrization, the cost on linear solver is also reduced. This can be explained by the fact that fewer Newton iterations are needed to converge.

**Table 2** Physical parameters and simulation scheme of FluidFlower simulation cases

Properties	Symbols	Values	Units
Reservoir temperature	$T$	293.15	K
Initial reservoir pressure	$p_0$	101,325	Pa
$\text{CO}_2$ viscosity	$\mu_{\text{CO}_2}$	$1.77\text{e-}5$	Pa.s
Brine viscosity	$\mu_b$	$1.01\text{e-}3$	Pa.s
Injection rate	$q$	10	ml/min
Injection time	$t_{\text{inj}}$	5/2.75	hours
Simulation time	$t_{\text{tot}}$	5	days

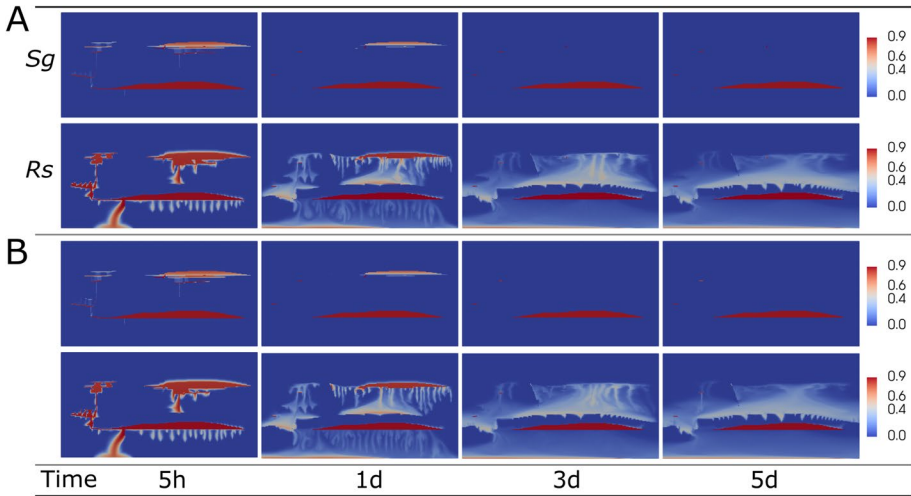
**Fig. 10** Comparison of simulation cost on the first day

### 5.3 Impacts of Hysteresis

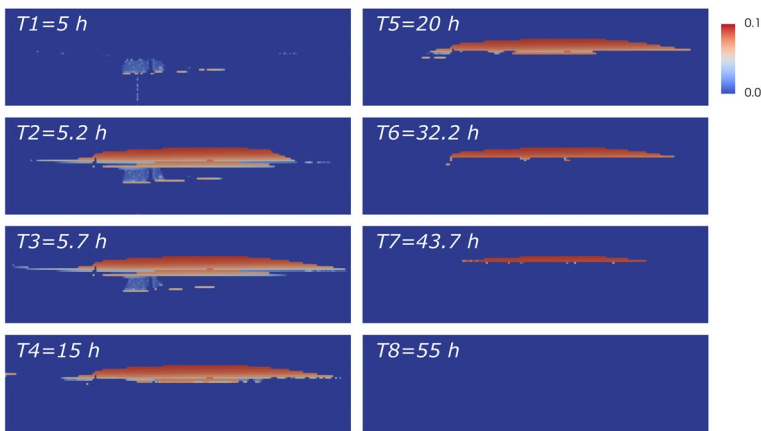
We model the hysteretic constitutive relations using the proposed parameterization method. The scanning curve surfaces are generated based on primary drainage and imbibition curves (shown in Fig. 9). On the other hand, in the case where hysteresis is neglected, we model it by assuming the drainage and imbibition processes follow the same curve. This assumption leads to zero residual gas saturation as the primary drainage curve starts from the saturation value of 0.

Figure 11 shows CO<sub>2</sub> saturation and dissolution ratio profiles at several representative time steps in the absence and presence of hysteresis effect. Minor differences between the two sets of maps indicate that including hysteresis does not have a pronounced impact. This is due to the fact that the primary drainage and imbibition curve is almost overlapped with each other in all sand types. As a result, even though flow may transition from primary curve to the scanning one, the deviation of relative permeability (or capillary pressure) value obtained from those two curves is insignificant. One may attribute the minor difference to loosely compacted sands used in the experiment, which deserves a further investigation. Nevertheless, previous experimental works have reported that hysteresis effect is pronounced in the sandstone: the primary drainage and imbibition curves deviate significantly (Akbarabadi and Piri 2013; Pini and Benson 2017). In those cases, residual trapping is one of the primary trapping mechanisms when injection stops (Ide et al. 2007; Wang et al. 2022).

Figure 12 shows the evolution of residual gas saturation in the upper gas cap over time. During injection period, very few cells have CO<sub>2</sub> in residual form because the flow is dominated by viscous force. Immediately after injection stops, the driving force within the system switches from viscous force to a balance between gravity and capillary forces. Consequently, the drainage process occurring in most cells is interrupted and transitioned to imbibition. In post-injection period, brine can be imbibed into CO<sub>2</sub> plume, which favors the trapping of CO<sub>2</sub> in residual form. Residual gas is further dissolved into brine: its region is found to shrink and even disappear as the convective transport proceeds.



**Fig. 11** Gas phase saturation and solution  $\text{CO}_2$ -brine ratio profiles obtained from the case **a** without and **b** with hysteresis effect



**Fig. 12** Residual gas saturation profiles within the upper gas plume in the presence of hysteresis effects

## 5.4 Impacts of Diffusion

To investigate the impact of diffusion, the diffusion coefficient of  $\text{CO}_2$  in liquid phase, i.e.,  $D_{\text{CO}_2,l}$ , is increased from 0 to positive values. Figure 13 shows the gas saturation and solution ratio maps for the three investigated cases. At the time when injection stops, the two cases considering diffusion effect do not show observable differences compared to the base case, because viscous force dominates the displacement process. During post-injection period, convective transport is enhanced in both lower and upper gas caps in the presence of diffusion. This is indicated by smaller gas caps at the same time. We also observe that interfaces between descending fingers and surrounding brine are more diffusive in cases (B) and (C).  $\text{CO}_2$  continues to leave the lower gas cap by dissolving into brine, and the gas cap almost disappears after 5 days.

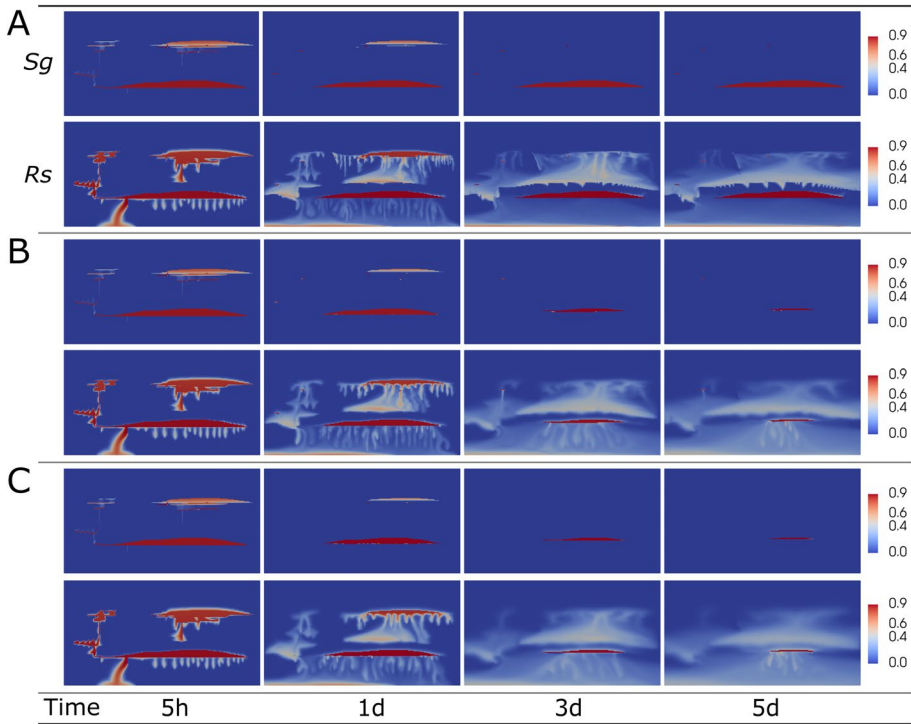


**Fig. 13** Gas phase saturation and solution CO<sub>2</sub>-brine ratio profiles in the absence or presence of diffusion. **a**, **b**, and **c** are obtained from  $D = 0 \text{ m}^2/\text{s}$  (base case),  $D = 2e - 9 \text{ m}^2/\text{s}$ , and  $D = 5e - 9 \text{ m}^2/\text{s}$ , respectively

To measure the degree of convective mixing,  $M$  is introduced:

$$M(t) = \int \left| \nabla \frac{x_c^w}{x_{c,\max}^w} \right| dx, \tag{20}$$

where  $x_c^w$  and  $x_{c,\max}^w$  denote the mass fraction of CO<sub>2</sub> in liquid phase and the dissolution limit, respectively. Figure 14a shows that inclusion of diffusion effect results in a remarkable increase of  $M$ . A larger diffusion coefficient leads to a stronger convective mixing under the lower gas cap, yet the stabilized value of  $M$  is close regardless of the strength of the diffusion coefficient. This finding is consistent with the quantification results of dissolution trapping in the lower gas cap. As shown in Fig. 14b, the largest amount of dissolved CO<sub>2</sub> is found in the case of  $D = 1e - 8 \text{ m}^2/\text{s}$ , and the three cases with nonzero diffusion coefficient tend to have similar increase rate at late stage.

## 6 Conclusion

In this work, a unified framework is developed to model the essential trapping physics of CO<sub>2</sub> storage in saline aquifers across varying time scales. Particularly, a parameterization method is proposed to describe hysteretic behavior of constitutive relations via interpolation of the parameterized space, which are constructed based on current saturation and the

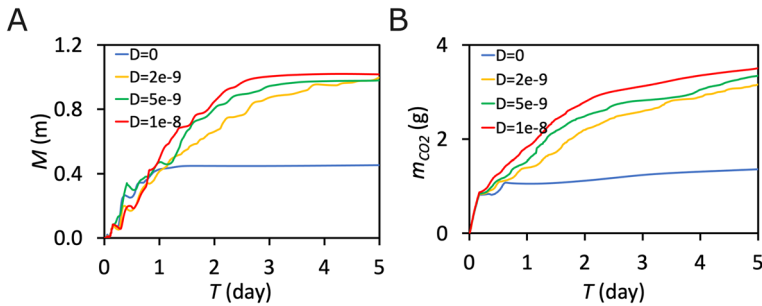


**Fig. 14** Quantification of convective mixing in the lower gas cap. **a**  $M$  value, and **b** amount of dissolution trapping

turning point saturation values. Moreover, analytical expressions are derived for thermodynamic equilibrium calculation using the black-oil fluid model. Partitioning of components into phases is readily obtained without performing standard flash calculations.

The proposed framework is validated by investigating the dynamics of gravity-induced convective transport. Results indicate that both the fingering pattern and the quantitative dissolution rate agree well with those reported in the literature. The numerical simulator is then applied to study the FluidFlower benchmark model with well-defined geological heterogeneity. Physical parameters, i.e., the permeability of different sand layers, are tuned such that the simulation results match physical observations from the tracer test. Results indicate that hysteresis effect does not have a great impact on the migration of plume in this specific setting, and most of the residually trapped  $\text{CO}_2$  is eventually dissolved into brine. Furthermore, inclusion of diffusion into the model enhances the convective mixing thereby increasing the amount of dissolution trapping. Our developed numerical model is shown to capture the relevant physical processes for  $\text{CO}_2$  storage in saline aquifers. Especially, it provides an efficient and accurate evaluation of residual trapping, which helps to assess when injected  $\text{CO}_2$  is trapped or stored in a more permanent form.

**Acknowledgements** Yuhang Wang was supported by the “CUG Scholar” Scientific Research Funds at China University of Geosciences (Wuhan) (Project No. 2022157). Ziliang Zhang acknowledges the financial support of China Scholarship Council (No. 202207720047). Hadi Hajibeygi was sponsored by the Dutch National Science Foundation (NWO) under Vidi Talent Program Project “ADMIRE” (Project No. 17509). We thank all ADMIRE members and its user committee for allowing us publish this paper. The code developed in this work is made open-source and accessible on <https://gitlab.com/DARSim>.

**Author Contributions** Conceptualization, YW, ZZ, HH; methodology, YW, ZZ, HH; software, YW, ZZ; investigation, YW, ZZ; writing—original draft preparation, YW, ZZ; writing—review and editing, CV, HH; supervision, CV, HH; project administration, CV, HH; funding acquisition, YW, HH

## Declarations

**Conflict of interest** The authors declare that they have no known competing financial interests or personal relationships that could have appeared to influence the work reported in this paper.

**Open Access** This article is licensed under a Creative Commons Attribution 4.0 International License, which permits use, sharing, adaptation, distribution and reproduction in any medium or format, as long as you give appropriate credit to the original author(s) and the source, provide a link to the Creative Commons licence, and indicate if changes were made. The images or other third party material in this article



are included in the article's Creative Commons licence, unless indicated otherwise in a credit line to the material. If material is not included in the article's Creative Commons licence and your intended use is not permitted by statutory regulation or exceeds the permitted use, you will need to obtain permission directly from the copyright holder. To view a copy of this licence, visit <http://creativecommons.org/licenses/by/4.0/>.

## References

- Akbarabadi, M., Piri, M.: Relative permeability hysteresis and capillary trapping characteristics of supercritical CO<sub>2</sub>/brine systems: an experimental study at reservoir conditions. *Adv. Water Resour.* **52**, 190–206 (2013)
- Boon, M., Matthäi, S.K., Shao, Q., et al.: Anisotropic rate-dependent saturation functions for compositional simulation of sandstone composites. *J. Petrol. Sci. Eng.* **209**(109), 934 (2022)
- Class, H., Ebigbo, A., Helmig, R., et al.: A benchmark study on problems related to CO<sub>2</sub> storage in geologic formations. *Comput. Geosci.* **13**(4), 409–434 (2009)
- Cusini, M., Fryer, B., van Kruijsdijk, C., et al.: Algebraic dynamic multilevel method for compositional flow in heterogeneous porous media. *J. Comput. Phys.* **354**, 593–612 (2018)
- Dai, Z., Xu, L., Xiao, T., et al.: Reactive chemical transport simulations of geologic carbon sequestration: methods and applications. *Earth Sci. Rev.* **208**(103), 265 (2020)
- De Paoli, M., Zonta, F., Soldati, A.: Dissolution in anisotropic porous media: modelling convection regimes from onset to shutdown. *Phys. Fluids* **29**(2), 026601 (2017)
- Duan, Z., Sun, R.: An improved model calculating CO<sub>2</sub> solubility in pure water and aqueous NaCl solutions from 273 to 533 K and from 0 to 2000 bar. *Chem. Geol.* **193**(3–4), 257–271 (2003)
- Elenius, M., Voskov, D., Tchelepi, H.: Interactions between gravity currents and convective dissolution. *Adv. Water Resour.* **83**, 77–88 (2015)
- Elenius, M.T., Nordbotten, J.M., Kalisch, H.: Convective mixing influenced by the capillary transition zone. *Comput. Geosci.* **18**(3), 417–431 (2014)
- Emami-Meybodi, H., Hassanzadeh, H.: Two-phase convective mixing under a buoyant plume of CO<sub>2</sub> in deep saline aquifers. *Adv. Water Resour.* **76**, 55–71 (2015)
- Emami-Meybodi, H., Hassanzadeh, H., Green, C.P., et al.: Convective dissolution of CO<sub>2</sub> in saline aquifers: progress in modeling and experiments. *Int. J. Greenhouse Gas Control* **40**, 238–266 (2015)
- Ershadnia, R., Wallace, C.D., Soltanian, M.R.: CO<sub>2</sub> geological sequestration in heterogeneous binary media: effects of geological and operational conditions. *Adv. Geo-Energy Res.* **4**(4), 392–405 (2020)
- Flemisch, B., Nordbotten, J.M., Fernø, M., et al.: The FluidFlower international benchmark study: process, modeling results, and comparison to experimental data. [arXiv:2302.10986](https://arxiv.org/abs/2302.10986), submitted to *Transport in Porous Media* (2023)
- Gunter, W., Perkins, E., Hutcheon, I.: Aquifer disposal of acid gases: modelling of water-rock reactions for trapping of acid wastes. *Appl. Geochem.* **15**(8), 1085–1095 (2000)
- Hajibeygi, H., Tchelepi, H.A.: Compositional multiscale finite-volume formulation. *SPE J.* **19**(02), 316–326 (2014)
- Hassanzadeh, H., Pooladi-Darvish, M., Elsharkawy, A.M., et al.: Predicting PVT data for CO<sub>2</sub>-brine mixtures for black-oil simulation of CO<sub>2</sub> geological storage. *Int. J. Greenhouse Gas Control* **2**(1), 65–77 (2008)
- Herring, A.L., Harper, E.J., Andersson, L., et al.: Effect of fluid topology on residual nonwetting phase trapping: implications for geologic CO<sub>2</sub> sequestration. *Adv. Water Resour.* **62**, 47–58 (2013)
- Hunt, J.R., Sitar, N., Udell, K.S.: Nonaqueous phase liquid transport and cleanup: 1. analysis of mechanisms. *Water Resour. Res.* **24**(8), 1247–1258 (1988)
- Ide, S.T., Jessen, K., Orr, F.M., Jr.: Storage of CO<sub>2</sub> in saline aquifers: effects of gravity, viscous, and capillary forces on amount and timing of trapping. *Int. J. Greenhouse Gas Control* **1**(4), 481–491 (2007)
- Jackson, S.J., Krevor, S.: Small-scale capillary heterogeneity linked to rapid plume migration during CO<sub>2</sub> storage. *Geophys. Res. Lett.* **47**(18):e2020GL088616 (2020)
- Juanes, R., Spiteri, E., Orr Jr, F., et al.: Impact of relative permeability hysteresis on geological CO<sub>2</sub> storage. *Water Resour. Res.* **42**(12) (2006)
- Killough, J.: Reservoir simulation with history-dependent saturation functions. *Soc. Petrol. Eng. J.* **16**(01), 37–48 (1976)
- Kou, Z., Wang, H., Alvarado, V., et al.: Method for upscaling of CO<sub>2</sub> migration in 3D heterogeneous geological models. *J. Hydrol.* **613**(128), 361 (2022)

- Krevor, S., de Coninck, H., Gasda, S.E., et al.: Subsurface carbon dioxide and hydrogen storage for a sustainable energy future. *Nat. Rev. Earth Environ.* pp 1–17 (2023)
- Land, C.S.: Calculation of imbibition relative permeability for two- and three-phase flow from rock properties. *Soc. Petrol. Eng. J.* **8**(02), 149–156 (1968)
- Lyu, X., Voskov, D., Rossen, W.R.: Numerical investigations of foam-assisted CO<sub>2</sub> storage in saline aquifers. *Int. J. Greenhouse Gas Control* **108**(103), 314 (2021)
- Metz, B., Davidson, O., De Coninck, H., et al.: *IPCC Special Report on Carbon Dioxide Capture and Storage*. Cambridge University Press, Cambridge (2005)
- Nordbotten, J.M., Flemisch, B., Gasda, S., et al.: Uncertainties in practical simulation of CO<sub>2</sub> storage. *Int. J. Greenhouse Gas Control* **9**, 234–242 (2012)
- Nordbotten, J.M., Fernø, M., Flemisch, B., et al.: Final Benchmark Description: FluidFlower International Benchmark Study. (2022). <https://doi.org/10.5281/zenodo.6807102>
- Oak, M., Baker, L., Thomas, D.: Three-phase relative permeability of Berea sandstone. *J. Petrol. Technol.* **42**(08), 1054–1061 (1990)
- Pini, R., Benson, S.M.: Capillary pressure heterogeneity and hysteresis for the supercritical CO<sub>2</sub>/water system in a sandstone. *Adv. Water Resour.* **108**, 277–292 (2017)
- Ranganathan, P., Farajzadeh, R., Bruining, H., et al.: Numerical simulation of natural convection in heterogeneous porous media for CO<sub>2</sub> geological storage. *Transp. Porous Media* **95**(1), 25–54 (2012)
- Ruprecht, C., Pini, R., Falta, R., et al.: Hysteretic trapping and relative permeability of CO<sub>2</sub> in sandstone at reservoir conditions. *Int. J. Greenhouse Gas Control* **27**, 15–27 (2014)
- Shao, Q., Boon, M., Youssef, A., et al.: Modelling CO<sub>2</sub> plume spreading in highly heterogeneous rocks with anisotropic, rate-dependent saturation functions: A field-data based numeric simulation study of Otway. *Int. J. Greenhouse Gas Control* **119**(103), 699 (2022)
- Snæbjörnsdóttir, S.Ó., Sigfússon, B., Marieni, C., et al.: Carbon dioxide storage through mineral carbonation. *Nat. Rev. Earth Environ.* **1**(2), 90–102 (2020)
- Spycher, N., Pruess, K.: CO<sub>2</sub>-H<sub>2</sub>O mixtures in the geological sequestration of CO<sub>2</sub>. ii. partitioning in chloride brines at 122–1000°C and up to 600 bar. *Geochimica et Cosmochimica Acta* **69**(13):3309–3320 (2005)
- Spycher, N., Pruess, K., Ennis-King, J.: CO<sub>2</sub>-H<sub>2</sub>O mixtures in the geological sequestration of CO<sub>2</sub>. i. assessment and calculation of mutual solubilities from 12 to 100°C and up to 600 bar. *Geochimica et Cosmochimica Acta* **67**(16):3015–3031 (2003)
- Steffy, D., Barry, D., Johnston, C.: Influence of antecedent moisture content on residual LNAPL saturation. *Soil Sediment Contam.* **6**(2), 113–147 (1997)
- Szulczewski, M., Hesse, M., Juanes, R.: Carbon dioxide dissolution in structural and stratigraphic traps. *J. Fluid Mech.* **736**, 287–315 (2013)
- Tsinober, A., Rosenzweig, R., Class, H., et al.: The role of mixed convection and hydrodynamic dispersion during CO<sub>2</sub> dissolution in saline aquifers: a numerical study. *Water Resour. Res.* **58**(3):e2021WR030494 (2022)
- Voskov, D.V., Tchelepi, H.A.: Comparison of nonlinear formulations for two-phase multi-component EoS based simulation. *J. Petrol. Sci. Eng.* **82**, 101–111 (2012)
- Wang, Y., Aryana, S.A., Allen, M.B.: An extension of Darcy's law incorporating dynamic length scales. *Adv. Water Resour.* **129**, 70–79 (2019)
- Wang, Y., Vuik, C., Hajibeygi, H.: Analysis of hydrodynamic trapping interactions during full-cycle injection and migration of CO<sub>2</sub> in deep saline aquifers. *Adv. Water Resour.* **159**(104), 073 (2022)
- Wen, B., Shi, Z., Jessen, K., et al.: Convective carbon dioxide dissolution in a closed porous medium at high-pressure real-gas conditions. *Adv. Water Resour.* **154**(103), 950 (2021)
- Yang, Z., Chen, Y.F., Niemi, A.: Gas migration and residual trapping in bimodal heterogeneous media during geological storage of CO<sub>2</sub>. *Adv. Water Resour.* **142**(103), 608 (2020)
- Zheng, T., Guo, B., Shao, H.: A hybrid multiscale framework coupling multilayer dynamic reconstruction and full-dimensional models for CO<sub>2</sub> storage in deep saline aquifers. *J. Hydrol.* **600**(126), 649 (2021)

**Publisher's Note** Springer Nature remains neutral with regard to jurisdictional claims in published maps and institutional affiliations.